POLITECNICO DI TORINO
Repository ISTITUZIONALE

Thin-lens equation in elasticity: Imaging with gradient-index phononic crystals

(Article begins on next page)

19 February 2025

Thin-lens equation in elasticity: Imaging with gradient-index phononic crystals

P.H. Beoletto [1,†] F. Nistri,[1] A.S. Gliozzi,[1] N.M. Pugno,[2,3] and F. Bosia [1,*]

[1] *Department of Applied Science and Technology, Politecnico di Torino, C.so Duca degli Abruzzi, 24, Torino 10129, Italy*

[2] *Laboratory for Bio-inspired, Bionic, Nano, Meta Materials and Mechanics, Department of Civil, Environmental and Mechanical Engineering, University of Trento, Trento 38123, Italy*

[3] *School of Engineering and Materials Science, Queen Mary University of London, Mile End Road, London E1 4NS, United Kingdom*

Many works in elasticity have exploited the concept of gradient-index (GRIN) lenses, borrowed from optics, for wave focusing and control. These effects are particularly attractive for cloaking, absorption, or energy-harvesting applications. Despite their potential, current lens designs suffer from limitations, mainly related to the difficulty of imaging pointlike sources. Here, we exploit an alternative GRIN lens design that enables a one-to-one correspondence between input and output phase and allows the focal length to be determined using the well-known thin-lens equation, effectively establishing an elastic equivalent of the convex lens in optics. This is demonstrated analytically, obtaining a bijective relation between the location of a pointlike source and its image. The results are also confirmed numerically and experimentally in an aluminum plate, in which the lens is realized by introducing rows of circular cavities of variable diameter. Moreover, a proof-of-concept experiment demonstrates the possibility of imaging sources of flexural waves at the centimeter scale with subwavelength resolution. This research can extend applications of elastic GRIN lenses to new fields such as imaging and nondestructive testing, in which the locations of defects can be identified by focusing the scattered field. Multiple sources can be imaged simultaneously, and the combined effects of multiple lenses can also be used to design more complex systems, opening new possibilities for the technological exploitation of elastic wave manipulation.

I. INTRODUCTION

The mathematical analogy between the laws governing electromagnetism and linear elasticity has often led researchers to draw inspiration from photonic devices to obtain similar effects in the field of elastic wave propagation. The first full band-structure calculations for periodic elastic composites were based on studies of photonic crystals [1], and since then, many aspects of interest in phononic crystals have evolved along similar lines [2]. The quest for wide-frequency band gaps exploiting Bragg or local resonances [3–7], the design of topological waveguides [8–11], and the development of gradient-index acoustics [12] highlight several similarities between the theory of elastic metamaterials and their optical counterparts. Although gradient-index lenses can be designed by modulating the thickness of the medium supporting the propagation [13–16], gradient-index (GRIN) phononic

crystals exploit local variations of the unit cell geometry to design a refractive index profile that induces the desired effect on the propagating acoustic wave in a specific frequency band; in subwavelength conditions (i.e., at low frequencies), these devices behave as homogeneous nondispersive materials whose effective properties are tuned by locally changing the geometry of the units [17]. While wave focusing can be achieved by exploiting negative refraction at frequencies above the first complete band gap [18–22], changing the radius of the holes modifies the phase velocity of all the modes, enabling operation across wide frequency bands [12] at low frequencies. Over the past decade, much attention has been dedicated to the idea of exploiting GRIN lenses to focus elastic waves by acting on the local phase of the propagating wave to obtain the desired interference effects [23,24]. A typical refractive index profile chosen for this kind of device is in the form of a hyperbolic secant [25], inspired by previous studies in gradient-index optics [26–28]; this profile allows to focus an incoming plane wave at a focal point and has mainly been used for energy-harvesting applications [29–34]. Several reports have proposed the use of circular

---

*Contact author: federico.bosia@polito.it
†Contact author: paolo.beoletto@polito.it

Lunenburg lenses to obtain similar plane wave focusing effects [35–38]. Both options allow unprecedented subwavelength focusing, which is unattainable with traditional elastic materials. Despite these attractive features, GRIN lenses are limited in their applicability. Hyperbolic secant profiles [23,24] are monodirectional, and they are only designed to focus incoming plane waves. Lunenburg lenses can be seen as omnidirectional [35], but their focusing properties are also limited to plane waves, and they do not display the ability to image finite objects. Maxwell's fish-eye elastic lenses have also been proposed [39,40], drawing inspiration from optics [41–43]; these can refocus the field generated by pointlike sources, but this effect is limited to sources located at the boundaries of the crystal.

In this paper, we propose an alternative GRIN lens design for out-of-plane flexural waves, exploiting the concept of "partitions" introduced in Ref. [44]. By separating neighboring rows of the photonic crystal, we prevent the waves propagating in one layer from interacting with those in adjacent layers, allowing a one-to-one correspondence between the output and input phases to be established. This condition allows us to determine the refractive index profile necessary for a lens with a desired focal length by compensating for the phase discrepancy related to propagation with the in-lens phase delay. Having determined the required parabolic phase profile for a correct phase delay to the incoming wave, we develop an analytical model in paraxial approximation, showing that this device mimics the simplest and most widely used optical device, i.e., a convex lens, and conforms to Snell's law for thin lenses, also known as the "lens maker's equation" [45], for which imaging conditions are obtained at a specific distance from the lens for a given source location. Given its similarities to an optical convex lens [46], the device proposed in this work is referred to as a "positive flat lens", as it maintains the same converging and imaging properties without requiring a curved shape. The device presented in this work can go beyond the limitations of existing GRIN lenses, allowing unprecedented flexibility in terms of applications. Exploiting the possibility of establishing a bijective relation between the object location and its image, it can map the prelens plane to the postlens plane. Thus, the novelty of this work lies in the demonstration of effective imaging of pointlike sources, regardless of their shape and location. Our approach includes a theoretical analytical to determine the focal properties of the lens, a numerical verification of the full-field elastic wave propagation problem and an experimental realization and characterization of the lens in lab tests.

II. RESULTS

A. Design of positive flat lenses

The lens design is based on a partitioned phononic crystal [44], which ensures that wave propagation in each "channel" is independent of that in the others. Thus, the phase delay imposed at a specific position y of the lens depends only on the refractive index $n(y)$ of that specific line, based on the bijective relation $\Delta\phi(y) = Wk_0 n(y)$, where W is the length of the acoustic path inside the lens and k_0 is the wavevector in the original material. The approach proposed to design a lens that is able to focus a plane wave at the coordinates $(f, 0)$, where f is the focal point, is to compensate for the postlens phase delay so that all acoustic paths contribute to constructive interference at this point. In general, the acoustic path crossing the lens at the coordinate y is characterized by the following phase components: $\phi_{\text{tot}}(y) = \phi_{\text{in}}(y) + \Delta\phi(y) + \phi_P(y)$, where ϕ_{in} is the input phase, $\Delta\phi$ is the phase delay imposed by the lens, and ϕ_P is the postlens phase related to the propagation towards a specific point. A lens designed to focus a plane wave needs to consider a constant input phase, and the total phase needs to be independent of y (i.e., independent of the acoustic path) to provide constructive interference. The postlens phase can be expressed as $\phi_P(y) = 2\pi k_0 d(y) = 2\pi k_0 \sqrt{y^2 + f^2}$. The phase delay imposed by the lens is then expressed as $\Delta\phi(y) = \Phi_0 - 2\pi k_0 \sqrt{y^2 + f^2}$. A parabolic refractive index profile leads to a parabolic postlens phase profile. In this work, we consider a lens [Figs. 1(a) and 1(b)] with focal length $f = 15$ cm and working frequency $\nu = 20$ kHz. The supporting medium is a thin aluminum plate of area 100 cm × 60 cm and thickness $d = 3$ mm. The partitions are $0.2-$ mm-wide slits separating the layers, and the unit cells of the phononic crystal are squares in the xy plane with side length $a = 1$ cm containing circular holes [Fig. 2(a)], whose radius r determines the refractive index [Figs. 1(c) and 1(d)]. The gap related to the presence of partitions does not affect the cell dimensions and shape, as it is added laterally, keeping the side length unchanged.

Eigenfrequency simulations imposing two-dimensional Bloch-Floquet quasiperiodicity in the xy plane are conducted for ten values of the filling factor $F = 2r/a$, sampling the Brillouin zone in the Γ–X direction. Full three-dimensional (3D) finite-element method simulations are carried out using COMSOL Multiphysics. Aluminum is modeled using the following parameters in the linear elastic constitutive law: density $\rho = 2700$ kg m^{-3}, Young's modulus $E = 70$ GPa, and Poisson's ratio $\nu_P = 0.33$. The cell is meshed by means of tetrahedral elements with a maximum size of 0.55 mm; these are automatically created by the software to preserve the geometry of the circular enclosure. The dispersion relation of the first antisymmetric bending mode A_0 undergoes a redshift, with its effect intensifying with increasing filling factor [Fig. 2(b)]. Assuming that the frequency ν of this flexural mode has a quadratic dependence on the wavevector [47] $\nu = C(F) \cdot k^2$, where C is a coefficient depending only on F, we obtain an expression for the refractive index $n(F) = k(F)/k_0 = \sqrt{C_0/C(F)}$; i.e., n increases monotonically with the filling
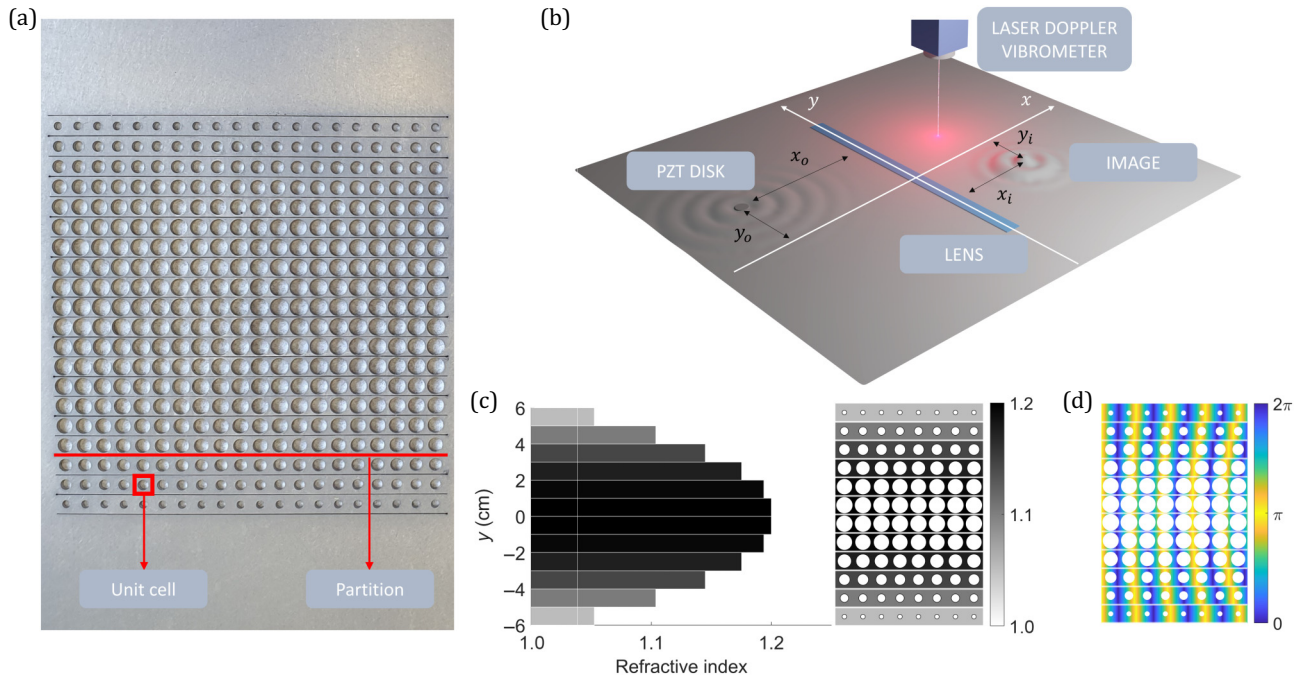
FIG. 1. (a) GRIN lens engraved into an aluminum plate, which was used for the experiments. (b) Rendering of the experimental setup: a piezoelectric disk is used to generate a propagating flexural wave and a laser doppler vibrometer is used to scan over the postlens area and detect the time-dependent out-of-plane displacement point by point. (c),(d) Representation of the effect of the grading of the refractive index on the phase of the flexural waves propagating inside the lens: cells having cavities with larger radii correspond to higher refractive indexes and shorter wavelengths.

factor [Fig. 2(c)]. This confirms that the relation between the filling factor and the phase delay is bijective. The refractive index is frequency independent for the A_0 mode, as the ratio between the wavevector in the crystal and in the supporting medium is unchanged for a given value of $C(F)$. A lens with focal length f can focus a plane wave at the coordinates $(f, 0)$. The lens compensates for the postlens phase delay such that all acoustic paths contribute to constructive interference at this point. The phase delay imposed by the lens is $\Delta\phi(y) = \Phi_0 - 2\pi k_0\sqrt{y^2 + f^2}$, where Φ_0 is a constant. This profile exhibits the same dependence on the direction y perpendicular to propagation as optical convex lenses, in which the phase delay is imposed by the radius of curvature. In the case of the considered flat lens with fixed width W, the same effect is obtained with the refractive index profile $n(y) = n_{\max} - \sqrt{y^2 + f^2}/W$.

Considering the generic object location (x_o, y_o) and image location (x_i, y_i), the phase associated with the acoustic paths of an elastic wave propagating from one point to the other is

$$\Phi_{\text{tot}} = 2\pi k_0\sqrt{y^2 + x_o^2} + \Phi_0$$
$$- 2\pi k_0\sqrt{y^2 + f^2} + 2\pi k_0\sqrt{y^2 + x_i^2}. \quad (1)$$

Following a similar approach to that used in optics [48], this equation can be simplified by applying a paraxial approximation, which holds when $y \ll x_o, f, x_i$. In these conditions, we can write

$$2\pi k_0\frac{y^2}{2}\left(\frac{1}{x_o} - \frac{1}{f} + \frac{1}{x_i}\right) = \Phi_{\text{tot}}. \quad (2)$$

The total phase at the location $(d_i, 0)$ is independent of the acoustic path only when

$$\frac{1}{x_o} + \frac{1}{x_i} = \frac{1}{f}. \quad (3)$$

This imaging condition is completely equivalent to the thin-lens formula, and it entails a one-to-one relationship between the x coordinate of the object and that of its image, given the focal length. In optics, this law can be obtained when the lens is thin, i.e., when the propagation inside the lens is almost uniaxial. In this approach, the equivalent concept is the partitioning of the lines of cells with different refractive indexes.

A final step in generalizing this model is to extend the approach to off-axis source positions (x_o, y_o). The distance r_{in} between the object and the lens at the coordinate y is

$$r_{\text{in}} = \sqrt{(x_o)^2 + (y_o - y)^2} \approx d_o + \frac{(y - y_o)^2}{x_o}. \quad (4)$$
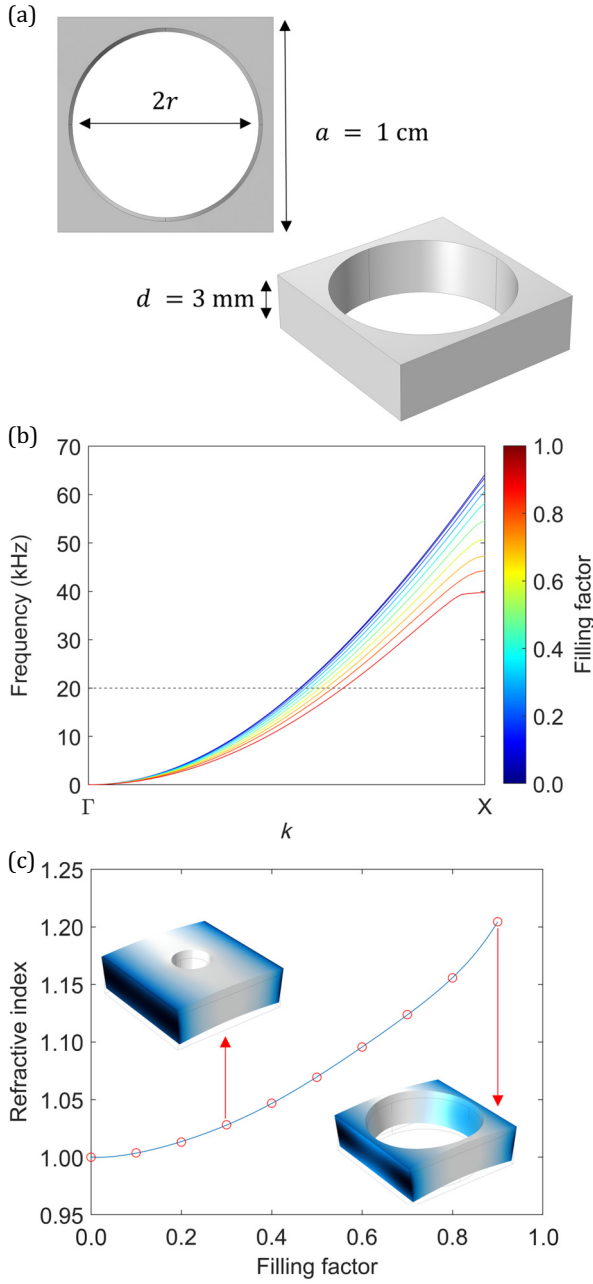
FIG. 2. (a) Representation of the unit cell: the filling factor is a parameter equal to $2r/a$, which is used to quantify the grading. (b) Redshift of the A_0 mode with increasing filling factor: eigenfrequency simulations with Bloch-Floquet conditions were run on unit cells with filling factors ranging from 0.1 to 0.9. (c) Bijective relation between the filling factor and the refractive index $n = k/k_0$.

This leads to an input phase profile that can be written as

$$\phi_{in}(y) = 2\pi k_0 \left(x_o + \frac{1}{x_o}(y^2 + y_o^2 - 2yy_o) \right). \quad (5)$$

The same holds in the postlens propagation phase term. To determine the imaging conditions, we require that the total phase associated to the propagation is a constant, Φ_{tot}, independent of the acoustic path:

$$\Phi_{tot} = 2\pi k_0 \left(\frac{1}{d_o} - \frac{1}{f} + \frac{1}{d_i} \right) \frac{y^2}{2}$$
$$+ 2\pi k_0 \frac{1}{2} \left(\frac{y_o^2}{d_o} + \frac{y_i^2}{d_i} \right) - 2\pi k_0 \left(\frac{y_o}{d_o} + \frac{y_i}{d_i} \right) y. \quad (6)$$

In the paraxial limit described by this formula, it is possible to observe that the total phase is independent of the acoustic path (i.e., Φ_{tot} is independent of y) when two imaging conditions are satisfied:

$$\frac{1}{x_o} + \frac{1}{x_i} = \frac{1}{f}, \quad (7)$$

$$y_i = -\frac{x_i}{x_o}y_o. \quad (8)$$

From these equations, we can observe that positive flat lenses are capable of creating images of pointlike objects: the (x_o, y_o) space is mapped into the (x_i, y_i) space with a functional dependence whose only parameter is the focal length. Equation (7) establishes the relationship between the position of the focal line and the distance of the source from the lens in the direction of propagation, while Eq. (8) states that their off-axis positioning depends upon the ratio of these distances.

B. Determination of lens focal length

The analytical model developed for the positive flat lens is initially verified through numerical and experimental approaches. The device is designed with a focal length of 15 cm, which is the parameter to be validated before checking its imaging properties. To do this, numerical full-field frequency-domain finite-element (FE) 3D simulations are performed using COMSOL Multiphysics. Perfectly matched layer (PML) boundary conditions are implemented on the edges of the 100×60 cm aluminum plate to minimize reflections at the boundaries. The PML is modeled with polynomial stretching, featuring a scaling factor of 1 and curvature parameter of 3. The lens area is meshed with tetrahedral elements, and the rest of the plate is meshed with eight-node hexahedral elements of maximum size 6 mm. The lens is positioned at the center of the plate, and a $20 - $ kHz excitation is imposed over a line to ensure a constant phase profile at the interface with the lens [Fig. 3]. The graded cell design gives rise to the parabolic refractive index profile shown in Fig. 4(a). The jumps in refractive index are not perceived as discontinuities because waves propagating in neighboring channels do not interfere with each other and a phase delay equal to 2π at the lens end is equivalent to 0. The first test is performed on a lens with an aperture of 30 cm, and for this design, the maximum displacement amplitude confirms the expected focal
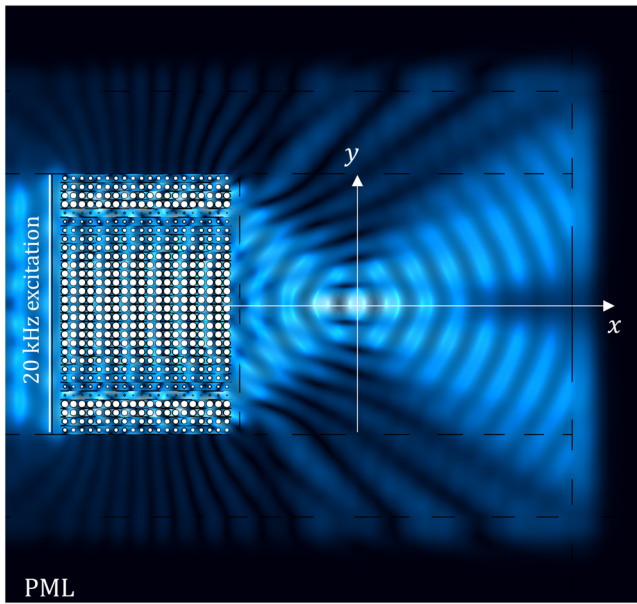
FIG. 3. Numerical simulation in frequency domain of the effect of a GRIN Lens designed to focus a 20 kHz plane wave with a focal length $f = 15$ cm (low displacement amplitude in black, high displacement amplitude in white).
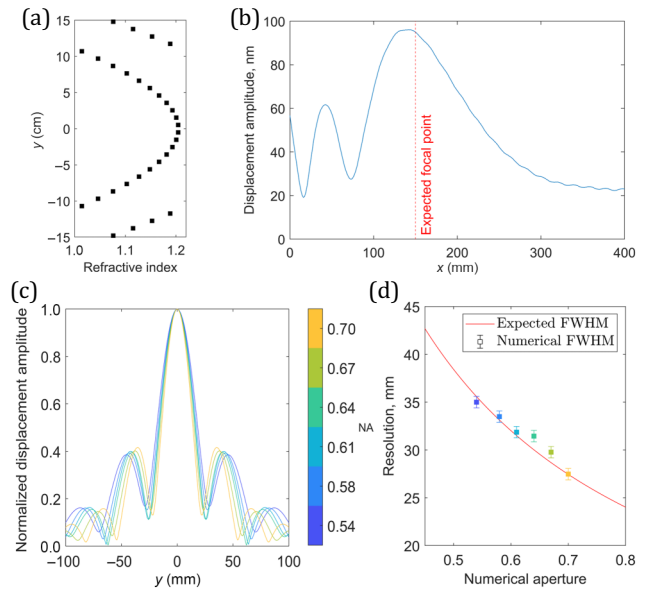

FIG. 4. (a) Refractive index profile of the lens under study. (b) Displacement amplitude profile in the propagation direction x obtained from a numerical simulation in the frequency domain. (c) Normalized displacement distributions in the focal plane for various numerical aperture values of the lens. (d) Resolution of the focal spot (calculated as its full width at half maximum) compared with the expected resolution.

length value [Fig. 4(b)]. The aperture of the lens has no influence on its focal length (see also Supplementary Material), but it does influence its resolution [48,49]. The Abbe diffraction limit defines the minimum resolvable size of an optical system as $d = \lambda/(2\text{NA})$, where $\text{NA} = n\sin(\theta)$ represents the numerical aperture. To ascertain whether our lens operates as a diffraction-limited system, the same simulation is performed on lenses with lateral dimensions ranging from 20 to 30 cm, i.e., numerical apertures in the range 0.55–0.71. The full width at half maximum of the focal spot in each test [Figs. 4(c) and 4(d)] is compared with the expected value of the diffraction limit, demonstrating quantitative agreement with theoretical predictions. Enhancing the system's resolution is possible by either increasing the aperture or using a higher refractive index in the postlens plane. It is always possible to include additional layers in the design to obtain a better resolution without modifying the focal point or the imaging properties of the lens.

Additionally, experimental validation of the lens's focal length was undertaken; the lens used for these experiments is the $20 - $cm-wide version. The lens design is fabricated on a thin aluminum plate via numerically controlled laser cutting. Piezoelectric transducers are taped to the plate and used to excite elastic waves. The wavefields are measured using a Polytec scanning laser Doppler vibrometer. The out-of-plane velocity of points belonging to a predefined grid is measured by moving the specimen in the xy

plane with two linear stages. Modeling clay is applied to the boundaries of the plate to partially reduce backscattering. The aim is to limit the steady-state effects on the wavefields. Due to the finite dimensions of the supporting medium, generating a plane wave at the lens entrance indicative of a source positioned infinitely distant proved challenging; therefore, experiments are performed in a time-reversed configuration, by placing the object at the focal point and detecting the plane wave that is expected to be generated on the other side of the lens. A piezoelectric transducer placed at a distance $f = 15$ cm from the lens is excited with a Gaussian pulse centered at 20 kHz with 10% bandwidth. This signal is sufficiently long to ensure the spatial coherence [50] of the field at the lens entrance. A laser Doppler vibrometer is used to scan over the postlens plane and record the time dependent out-of-plane displacement at each point (Fig. 5), which confirms the propagation of a plane wave. To check the radius of curvature of the wavefront, the signal at each point is Fourier transformed, and the $20 - $ kHz component is analyzed. Apart from a small deviation at the edges, which is linked to the background signal propagating out of the lens, the phase profile indicates that the wavefronts are planar (see Fig. 5 and Appendices). Thus, both numerical simulations and experiments corroborate the analytical design's focal length prediction for the device.
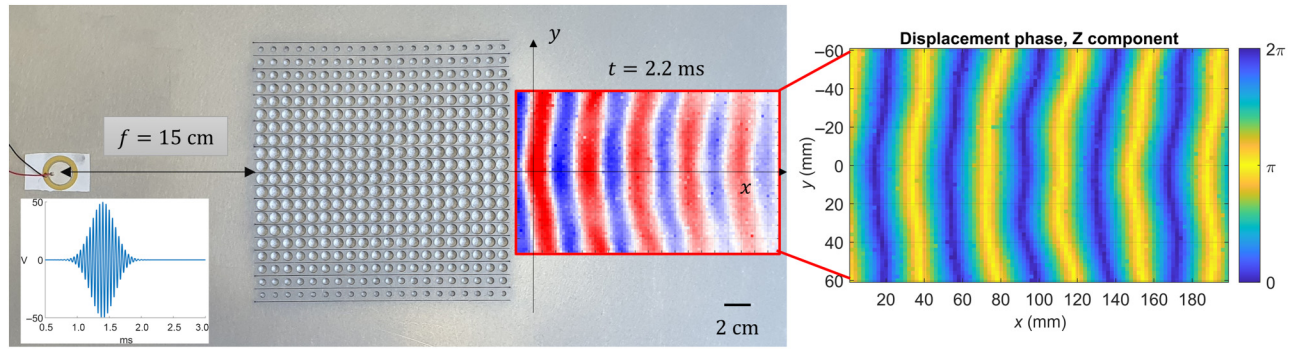
FIG. 5. Experimental validation of the focalization properties of the lens: a piezoelectric source is placed at the focal point of the lens at a distance $f = 15$ cm, and a snapshot of the plane wave propagating in the postlens plane is shown. The input signal is a Gaussian pulse centered at 20 kHz with a 10% bandwidth. The plot on the right shows the phase of the $20 -$ kHz component of the signal measured in the postlens plane, with planar wavefronts.

C. Imaging pointlike sources

Positive GRIN lenses are not only capable of focusing energy; their working principle also enables the imaging of objects and the reconstruction of their locations. Equations (7) and (8) show that the only parameter determining the relation between source and image positions is the focal length f, whose value has been shown to be consistent with the design predictions, both numerically and experimentally, in the previous section. For this given value of the focal length, a one-to-one relation between the object and image locations exists. To demonstrate the imaging capability of the device, numerical and experimental results are compared with analytical predictions.

From Eqs. (7) and (8), it follows that $x_i = (x_o f)/(x_o - f)$. This relation holds if the object is located at a distance larger than the focal length, since for smaller distances, the field does not converge to an image. A set of values of x_o around $2f$ is selected, ranging from 27 to 34 cm. Frequency-domain FE simulations are carried out using COMSOL Multiphysics with a point excitation at a frequency of 20 kHz for each value of x_o, and the same process is replicated experimentally using a piezoelectric disk as a source. The object is located along the central axis ($y_o = 0$), and displacements in the postlens area are studied on the same line. Numerically, the value of x_i is determined as the distance from the lens of the maximum of the out-of-plane component of the displacement amplitude. In experiments, a Fourier transform is performed on the time-domain signal measured at each point along the line, and the amplitude of the $20 -$ kHz component of the signal is selected to determine the maximum value. The analytical predictions are confirmed both by the experiments and by the numerical simulations [Fig. 6(a)]. The numerical and experimental results indicate steplike behavior in the relation between the object and image locations: the values of x_i appear to form a discrete set, attributable to the finite

size of the supporting medium, resulting in the presence of a backscattered wave. The reflections from the sides of the plate create an interference pattern in steady-state conditions, the maxima of which occur at intervals of $\lambda/2$ along the direction of propagation. This effect, superposed on the actual working principle of the device, is also accounted for in the simulations, where the actual plate geometry is considered. Figure 6(b) shows the map of the experimentally detected displacement amplitude with the source located at $x_o = 37$ cm. The fringes in this image correspond to the maxima of interference with the reflected wave. The map of the phase [Fig. 6(c)] indicates that the image is located in the region where the converging wavefront begins to diverge. The relation between the off-axis positioning of the source and of the image is also verified. The lens can operate in both magnification and demagnification regimes. When an object is located at a distance $x_o < 2f$ from the lens, the ratio $x_i/x_o > 1$ applies; in this condition, distances are increased, and the lens works in the magnification regime. The opposite is true for $x_o > 2f$, representing the demagnification regime. For $x_o = 2f$, the object is precisely mirrored at the focal line ($y_i = -y_o$). Three sets of experiments are conducted both in a numerical and experimental environment, for $x_o = 28$, 30, and 32 cm, i.e., $x_o < 2f$, $x_o = 2f$, and $x_o > 2f$. In each condition, the amplitude profile is analyzed at the corresponding focal line, with the source placed at the y_o values ranging from -4 to 4 cm. The position y_i of the peak of the displacement amplitude of the $20 -$ kHz component determines the image location. Figure 6(d) demonstrates a significant correlation between the experimental results and the analytical predictions of Eq. (8). As expected, the distances are either magnified or demagnified depending on the operational state of the lens [Fig. 6(e)]. Numerical simulations [Fig. 6(f)] confirm the experimental results (see also Appendices); therefore, the model for positive GRIN lenses is verified, and the
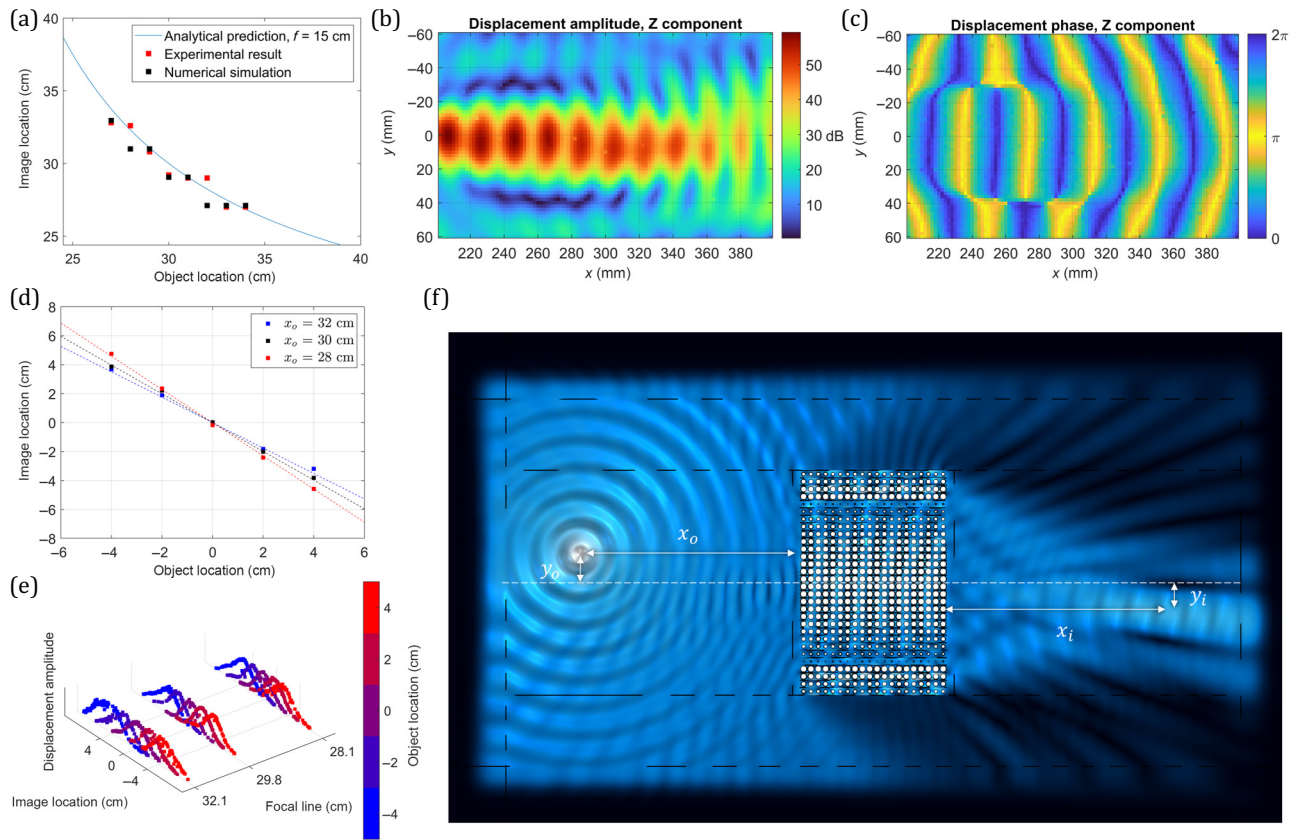
FIG. 6. (a) Comparison between analytical model, numerical simulations, and experimental results for the imaging of a pointlike source located at different distances from the lens. The image location corresponds to the point of maximum amplitude of the $20 - \mathrm{kHz}$ component of the propagating wave along the central line in the postlens plane. (b),(c) Postlens map of the amplitude and phase of the $20 - \mathrm{kHz}$ component of the signal generated with a source located at $x_o = 37$ cm and $y_o = 0$ cm. (d),(e) Results of imaging experiments with the source located off the central axis and the analytical expectations: three sets of experiments with $x_o = 28,\ 30,$ and 32 cm are performed, measuring the output at the specific focal line x_i, and the peak location of each measurement is compared with the expected $y_i = -(x_i/x_o)y_o$. (f) Numerical frequency-domain simulation of the lens imaging a source located at $(x_o = 30\,\mathrm{cm}, y_o = 4\,\mathrm{cm})$.

imaging properties of the device are fully respected for pointlike sources.

D. Localization of objects

The imaging capability of the positive GRIN lens can be extended from piezoelectric pointlike sources to any object that interacts with the wavefield propagating in the prelens area. In this section, a localization technique for pointlike defects is tested, based on the focalization and imaging properties of the lens. The localization of defects relies on the fact that there is a one-to-one relation between the position of a source and its image. While it is possible that existing gradient-index lenses induce a focalization effect on the field scattered from a defect, there is no documented way to extract information about its location from the amplitude distribution of the postlens field.

In the experiment, two cubic magnets [Figs. 7(a) and 7(b)] are placed at opposing positions on the upper and lower sides of the plate to create a local scattering obstacle

[51] to the wavefield at this location. A defect-free reference of the amplitude distribution of the signal is acquired, enabling a comparison of amplitude variations when the defect is introduced. An initial set of experiments is run with the defect located at $x_d = 32$ cm and four different values of y_d from -4 to 4 cm [Fig. 7(c)]. The amplitude shift is measured at the corresponding focal line $x_i = 28.2$ cm, where the effect of the object is expected to be focalized. Figure 7(c) shows that the peak of the amplitude shift is localized at position y_i, as predicted by the lens model. For the magnet placed at $y_d = -4$ cm, the expected image location is $y_i = 3.5$ cm, as observed in the experiments.

A final experiment is performed to directly test the resolution of the system by simultaneously placing two defects on the same line [Figs. 8(a)–8(c)]. The distances of the objects in the three experiments are 8, 6, and 4 cm, with corresponding expected distances at the image line of 7, 5.25, 3.5 cm. The objects are well resolved in the first two configurations (Fig. 8), but they cannot be distinguished in the last one [Fig. 8(c)]. Several mechanisms
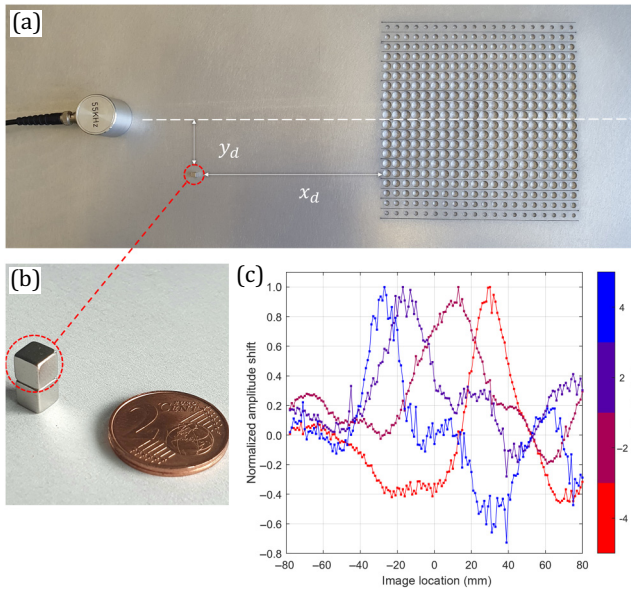
FIG. 7. (a) Setup of the defect-imaging experiment: the defect is located at (x_d, y_d), and the signal in the focal line $x_i = f \cdot x_d/(x_d - f)$ is compared with a defect-free reference to check for variations in the amplitude profile that was previously measured. (b) Magnetic cubes used as defect sources: the pressure on the plate generated by the magnetic attraction between the two cubes generates a local variation in the mechanical properties. (c) Images of defects located in different positions observed on the focal line: the amplitude shift is the difference of the current field with respect to the defect-free field.

need to be considered in evaluating the resolution of this system. First, we must consider the width of the lens, which defines the numerical aperture and thus sets the diffraction limit. Second, the source used in this configuration generates a spherical wave: the field interacting with the object has nonzero components in the direction perpendicular to propagation as the magnets are placed off axis.

As the object approaches the central axis, the reduced value of k_y in the scattered field increases the minimum distinguishable feature size, explaining why objects placed only 4 cm apart cannot be resolved.

III. DISCUSSION

In conclusion, we have proposed a design procedure for the elastic counterpart of an optical convex lens based on gradient-index phononic crystals. The gradient-index designs that are currently available in the domain of elasticity are effective for focusing energy, but their working conditions are either limited to a specific direction of incoming wavefield or a specific source location. These limits are overcome by the device proposed in this work: the positive flat lens is the first phononic-crystal-based device that is able to create an image of a source of elastic waves regardless of its shape and location. The analytical model for the positive flat lens predicts that the device can create images of objects in a location unequivocally determined by its focal length. Both numerical simulations and experiments performed with pointlike sources confirm the design predictions in terms of both image location and resolution, validating the reliability of the underlying physical model. Moreover, the imaging capabilities of the lens were tested in a scattering configuration: using mechanical defects generated by the local pressure of two magnets, the lens has been shown to be capable of simultaneously localizing more than one object.

This work opens a range of potential applications. The first is to exploit focusing for energy harvesting or for material signal processing in low-power devices, because the simple design of the lens means it is amenable to miniaturization. Another possibility is related to the fact that the lenses can be used to magnify and demagnify objects, depending on their focal properties. This can be very useful, for example, in nondestructive testing applications
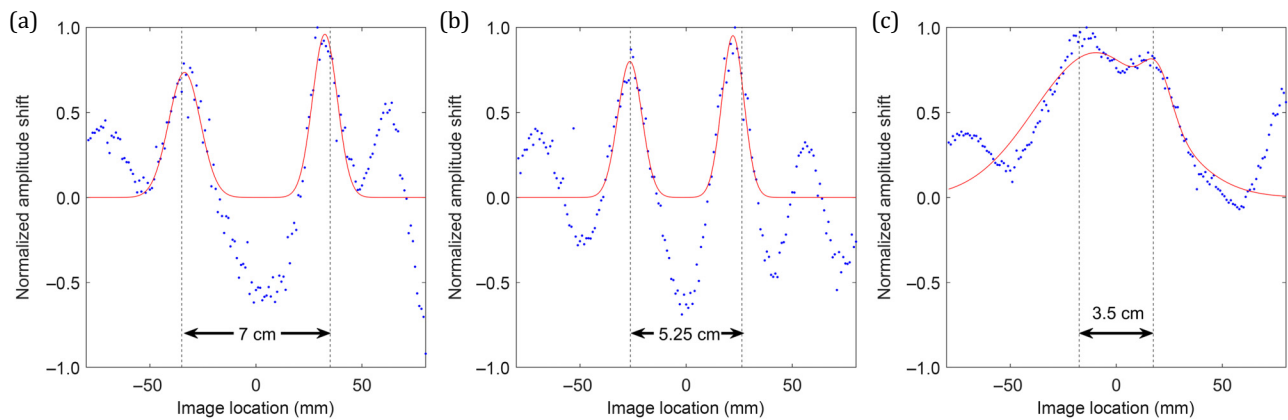

FIG. 8. (a)–(c) Peaks generated by the simultaneous presence of two defects located at distances of 8, 6, and 4 cm: in the last case, the distance is comparable to the wavelength $\lambda = 3.75$ cm, and the two defects cannot be distinguished. The blue dots represent the experimental data, and the red solid lines are fits to these data using the sum of two Gaussian functions.

when the inspected area is very large or very small, or difficult to access. An appropriate lens design can allow a scaled image of the target region to be generated in a convenient adjacent region. Finally, the combined effects of multiple lenses can also be used to design more complex systems for the control of flexural wave propagation, such as in elastic microscopes.

The convex lens, although simple in design, revolutionized the field of light manipulation and paved the way for advanced applications. The positive flat lens also has the potential to have a considerable impact, opening up new possibilities in the domain of elasticity.

APPENDIX A: ANALYTICAL MODEL OF THE POSITIVE FLAT LENS

The phase delay imposed at a specific position y of the lens depends only on the width W and on the refractive index $n(y)$ of the specific line

$$\Delta\phi(y) = Wk_0 n(y).$$

This makes it possible to design any lens given a desired phase profile, with no limitations except for the discretization imposed by the dimensions of the unit cell. The width of the lens is imposed by the fact that the whole phase domain needs to be covered, so the lines with maximum refractive index and the pure material need to have a phase delay of 2π:

$$W = \frac{2\pi}{k_0 n_{\max}}.$$

The approach proposed to design a lens that is able to focus a plane wave at the coordinates $(f, 0)$, where f is the focal point, is to compensate for the postlens phase delay so that all acoustic paths contribute to constructive interference at this point.

In general, the acoustic path crossing the lens at the coordinate y is characterized by the following phase components (Fig. 9):

$$\phi_{\text{tot}}(y) = \phi_{\text{in}}(y) + \Delta\phi(y) + \phi_P(y),$$

where ϕ_{in} is the input phase, $\Delta\phi$ is the phase delay imposed by the lens, and ϕ_P is the postlens phase related to the propagation toward a specific point. A lens designed to focus a plane wave needs to consider a constant input phase, and the total phase needs to be independent of y, i.e., independent of the acoustic path, to provide constructive
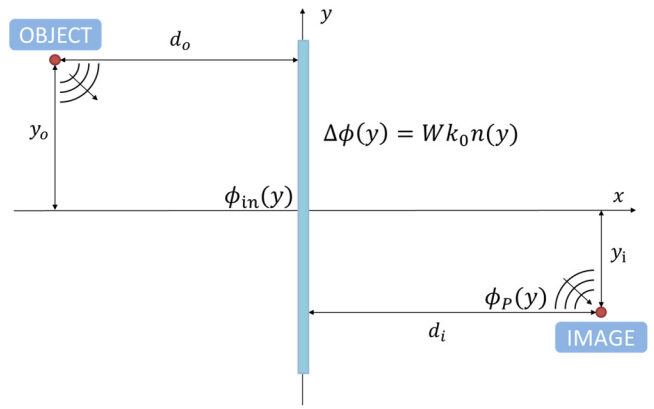

FIG. 9. Diagram illustrating the phases involved in the lens system.

interference:

$$\Delta\phi(y) + \phi_P(y) = \Phi_0.$$

The postlens phase can be expressed as

$$\phi_P(y) = 2\pi k_0 d(y) = 2\pi k_0 \sqrt{y^2 + f^2}.$$

The phase delay imposed by the lens is then

$$\Delta\phi(y) = \Phi_0 - 2\pi k_0 \sqrt{y^2 + f^2}.$$

This profile exhibits the same dependence on the direction perpendicular to propagation as optical convex lenses, in which the phase delay is imposed by the radius of curvature. In the case of the considered flat lens with fixed width W, the same effect is obtained with the refractive index profile

$$n(y) = \frac{\Delta\phi(y)}{Wk_0} = n_{\max} - \frac{\sqrt{y^2 + f^2}}{W}.$$

The previous treatment is limited to the case in which the input phase profile is constant, which limits the working conditions to sources at a large distance from the lens. If the source is modeled as pointlike, at a finite distance, the term $\phi_{\text{in}}(y)$ cannot be omitted. Below, we show that a one-to-one relation between the object (source) position and the image position can be obtained.

A first extension of the treatment is to consider a pointlike source located at $(-d_o, 0)$ along the central line of the lens and to study the phase of the wave propagating to the point $(d_i, 0)$. In these conditions,

$$\begin{aligned}
\phi_{\text{tot}}(y) &= \phi_{\text{in}}(y) + \Delta\phi(y) + \phi_P(y) \\
&= 2\pi k_0 \sqrt{y^2 + (-d_o)^2} + \Phi_0 - 2\pi k_0 \sqrt{y^2 + f^2} \\
&\quad + 2\pi k_0 \sqrt{y^2 + d_i^2}.
\end{aligned}$$

As in the previous case, the condition for constructive interference is that the total phase related to the propagation must be independent of the acoustic path:

$$2\pi k_0 \sqrt{y^2 + d_o^2} - 2\pi k_0 \sqrt{y^2 + f^2} + 2\pi k_0 \sqrt{y^2 + d_i^2} = \Phi_{\text{tot}}.$$

Following a similar approach to that used in optics, we can simplify the equation by applying a paraxial approximation, which holds when $y \ll d_o, f, d_i$. In these conditions, we can write

$$2\pi k_0 \left(d_o \sqrt{1 + \frac{y^2}{d_o^2}} - f\sqrt{1 + \frac{y^2}{f^2}} + d_i \sqrt{1 + \frac{y^2}{d_i^2}} \right)$$

$$\approx 2\pi k_0 \left(\frac{y^2}{2d_o} - \frac{y^2}{2f} + \frac{y^2}{2d_i} \right),$$

$$2\pi k_0 \frac{y^2}{2} \left(\frac{1}{d_o} - \frac{1}{f} + \frac{1}{d_i} \right) = \Phi_{\text{tot}}.$$

The total phase at the location $(d_i, 0)$ is independent of the acoustic path only when

$$\frac{1}{d_o} + \frac{1}{d_i} = \frac{1}{f}.$$

This imaging condition is completely equivalent to the thin-lens formula, and it contains a one-to-one relationship between the x coordinate of the object and that of its image, given the focal length, as shown in Fig. 10. In optics, this law can be obtained when the lens is thin, i.e., when the propagation inside the lens is almost uniaxial. In the present approach, the equivalent concept is the partitioning of the lines of cells with different refractive indexes.

A final step in generalizing this model is to extend the approach to off-axis source positions $(-d_o, y_o)$ and to study the phase at a postlens point (d_i, y_i). The distance r_{in} between the object and the lens at the coordinate y is

$$r_{\text{in}} = \sqrt{(-d_o)^2 + (y_o - y)^2} \approx d_o + \frac{(y - y_o)^2}{d_o}.$$

This leads to an input phase profile that can be written as

$$\phi_{\text{in}}(y) = 2\pi k_0 \left(d_o + \frac{1}{d_o}(y^2 + y_o^2 - 2yy_o) \right).$$

The same holds in the postlens propagation phase term:

$$\phi_P(y) = 2\pi k_0 \left(d_i + \frac{1}{d_i}(y^2 + y_i^2 - 2yy_i) \right).$$

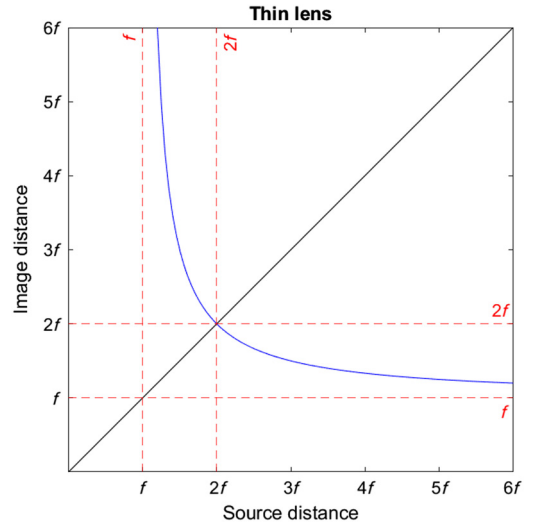As in the previous cases, to determine the imaging conditions, we require that the total phase associated with the

FIG. 10. Image position as a function of the source distance (d_i vs. d_o), as derived from the thin-lens formula $d_i = \frac{d_o f}{d_o - f}$.

propagation is a constant, Φ_{tot}, independent of the acoustic path:

$$\Phi_{\text{tot}} = +2\pi k_0 \left(d_o + \frac{1}{d_o}(y^2 + y_o^2 - 2yy_o) \right) - 2\pi k_0 \frac{y^2}{2f}$$

$$+ 2\pi k_0 \left(d_i + \frac{1}{d_i}(y^2 + y_i^2 - 2yy_i) \right),$$

$$\Phi_{\text{tot}} = 2\pi k_0 \left(\left(\frac{1}{d_o} - \frac{1}{f} + \frac{1}{d_i} \right) \frac{y^2}{2} - \left(\frac{y_o}{d_o} + \frac{y_i}{d_i} \right) y \right)$$

$$+ \pi k_0 \left(\frac{y_o^2}{d_o} + \frac{y_i^2}{d_i} \right).$$

This results in two imaging conditions that determine a one-to-one mapping of the object position $(-d_o, y_o)$ in the postlens plane at the point (d_i, y_i), namely:

$$\frac{1}{d_o} + \frac{1}{d_i} = \frac{1}{f}, \quad y_i = -\frac{d_i}{d_o} y_o.$$

From these equations, we can see that this flat gradient-index phononic crystal follows identical working principles to those of an optical convex lens. When the source is located at a distance $d_o > 2f$, the lens works in the magnification regime: in this case $d_i < d_o$, which means that on the image line, $|y_i| > |y_o|$. Demagnification conditions are met when $f < d_o < 2f$.

APPENDIX B: FREQUENCY INDEPENDENCE OF THE REFRACTIVE INDEX

Considering the dispersion relation of the first antisymmetric bending mode A_0, it is possible to assume

that the frequency ν has a quadratic dependence on the wavevector $\nu = C \cdot k^2$, where C is a constant depending on the mechanical properties of the supporting medium and its geometry. Figure 11(a) shows the dispersion curves obtained numerically using COMSOL Multiphysics for the unit cells presented in the main text.

When dealing with unit cells with different filling factors F, we can write their dispersion relation as $\nu(F) = C(F) \cdot k^2$, where the coefficient C depends on F. The refractive index for a specific filling factor at a given frequency ν is $n(F, \nu) = k(F, \nu)/k_0(\nu)$, where $k_0(\nu)$ is the wavevector relative to the frequency ν in the propagating medium (the unit cell with a null filling factor). Considering that $k(F, \nu) = \sqrt{\nu/C(F)}$ and $k_0(\nu) = \sqrt{\nu/C_0}$, we can write

$$n(F, \nu) = \frac{k(F, \nu)}{k_0(\nu)} = \frac{\sqrt{\nu/C(F)}}{\sqrt{\nu/C_0}} = \sqrt{\frac{C_0}{C(F)}} = n(F).$$

Under the assumption of a quadratic dispersion relation, the dependence of n on the frequency ν disappears. It is possible to say that the refractive index is frequency independent for the A_0 mode, as the ratio between the wavevector in the crystal and in the supporting medium is unchanged for a given value of $C(F)$, regardless of ν.

This analytical demonstration is also supported by numerical results. Starting from the dispersion curves obtained using eigenfrequency simulations and reported in Fig. 11(a), the refractive index for each value of filling factor was calculated for a set of frequencies ranging from 1 to 39 kHz, i.e., over a bandwidth of 190% around 20 kHz, which covers most of the frequencies of the A_0 mode of this structure. In Fig. 11(b) we can observe the standard deviation of the values of refractive index around the average computed for each filling factor. The frequency independence is clear for lower values of filling factor, while a small deviation becomes apparent as the filling factor approaches $F = 0.9$. This is related to the fact that these branches deviate from a quadratic trend as they approach the X point in the Brillouin zone (frequencies close to 39 kHz). Overall, considering that the bandwidth used for the calculation was quite broad, the numerical results strongly support the frequency independence of the refractive index.

APPENDIX C: ANIMATIONS

This appendix contains animations related to the experimental and numerical results, showing either information related to the temporal evolution of the system or highlighting the differences in the response of the lens under different working conditions.

In Video 1, the measurement presented in Fig. 5, which illustrates the generation of a plane wave from a source located at the focal point, is shown in the time domain.
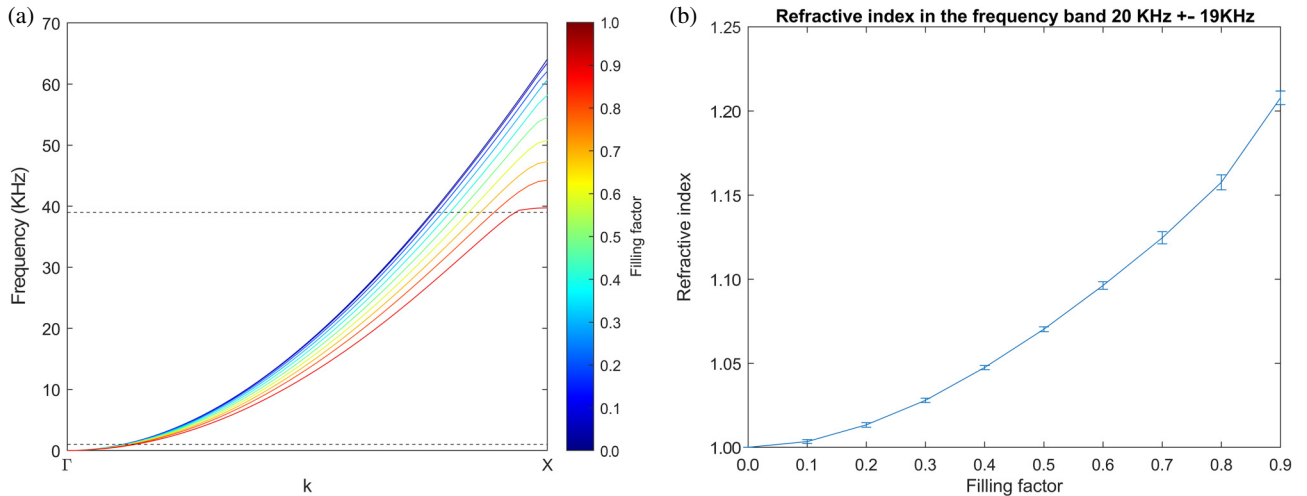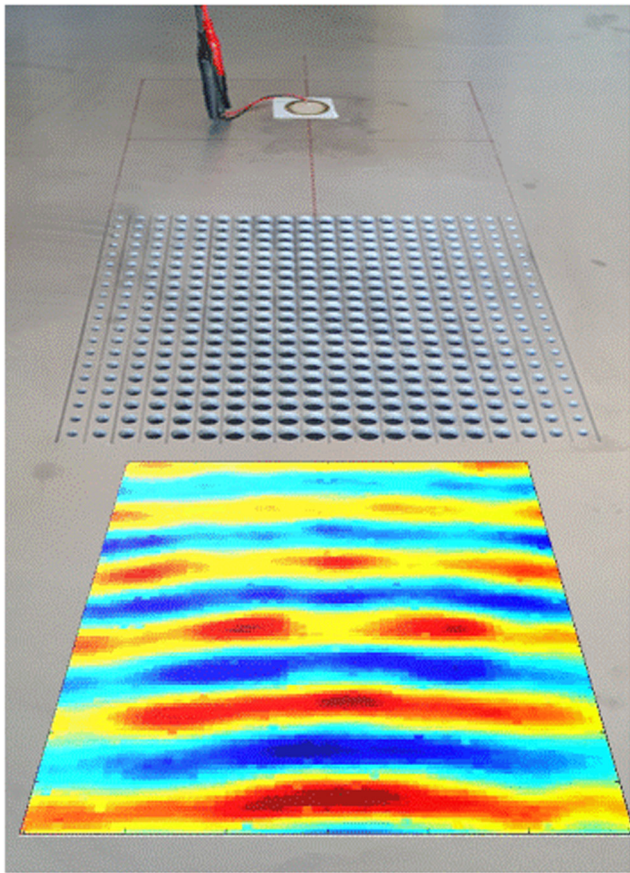

FIG. 11. (a) Dispersion curves for different values of filling factor obtained with eigenfrequency simulations in COMSOL Multiphysics. The unit cells are squares in the xy plane with side length $a = 1$ cm and circular holes. Their depth in the vertical direction is 3 mm. Aluminum is modeled using the following parameters: density $\rho = 2700 \, \text{kg m}^{-3}$, Young's modulus $E = 70$ GPa, and Poisson's ratio $\nu_P = 0.33$. The dashed lines are the limits of the frequency region that is taken into account to demonstrate the frequency independence of the refractive index. (b) The solid line shows the average values of refractive index calculated from the numerical dispersion curves taking into account a frequency band in the range 1 to 39 kHz. The error bars shows the standard deviation of the distribution of values of refractive index for each value of filling factor.
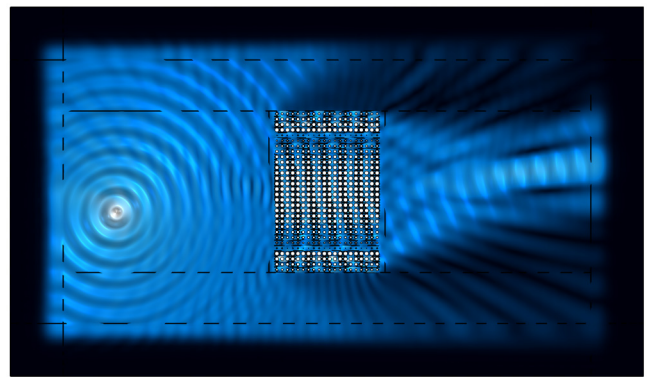
VIDEO 3. Full-field simulations of the system with different positions of pointlike source away from the central axis.

VIDEO 1. Animation showing the displacement amplitude of the field propagating after the action of the positive lens. The source is located at the focal point at a distance $f = 15$ cm, and the gradient of the refractive index causes the wavefront to become planar in the postlens plane. From blue to red, the color map ranges from negative to positive out-of-plane displacement.

aperture of the lens that are taken into consideration for these simulations in the frequency domain range from 20 to 30 cm.

In Video 3, it is possible to observe the action of the lens on the field generated by a source located in several off-axis positions (as presented in the main text in Fig. 6). Video 4 shows the same simulation for a lens based on the hyperbolic profile design procedure; in this case, some focalization effect on the incoming wave is present due to the gradient of refractive index, but it is not possible to predict the position of a source from that of an image. In other words, the wavefront is modified by the presence of the lens, but the lens does not create an image of the source.

Video 2 shows the effect of the numerical aperture on the width of the focal spot. As shown in Fig. 4 a wider aperture enhances the resolution. The dimensions of the
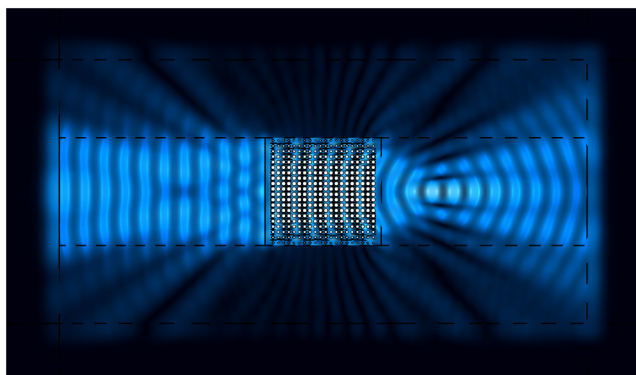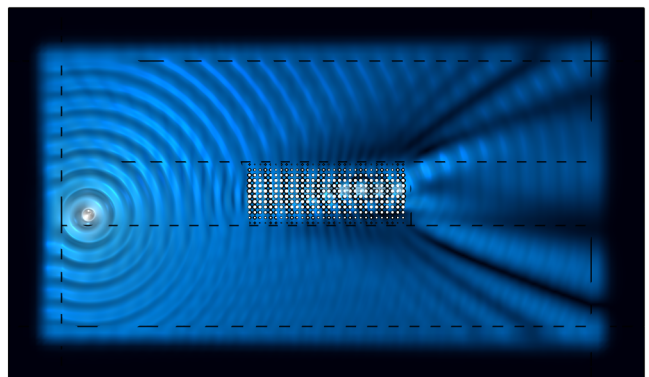

VIDEO 2. Animation showing the effect of the numerical aperture on the dimensions of the focal spot: a wider aperture enhances the resolution of the system.

VIDEO 4. Full-field simulations of a lens based on hyperbolic secant refractive index profile with equivalent focalization properties with respect to the positive lens studied in the main text (i.e., a focal length equal to 15 cm). The animation shows the effect of the lens on the fields generated by pointlike sources in several positions.

[1] M. S. Kushwaha, P. Halevi, L. Dobrzynski, and B. Djafari-Rouhani, Acoustic band structure of periodic elastic composites, Phys. Rev. Lett. **71,** 2022 (1993).

[2] Y. Pennec, J. O. Vasseur, B. Djafari-Rouhani, L. Dobrzyński, and P. A. Deymier, Two-dimensional phononic crystals: Examples and applications, Surf. Sci. Rep. **65,** 229 (2010).

[3] V. F. Dal Poggetto, F. Bosia, M. Miniaci, and N. M. Pugno, Band gap enhancement in periodic frames using hierarchical structures, Int. J. Solids Struct. **216,** 68 (2021).

[4] S. Chen, G. Wang, and Y. Song, Low-frequency vibration isolation in sandwich plates by piezoelectric shunting arrays, Smart Mater. Struct. **25,** 125024 (2016).

[5] A. O. Krushynska, M. Miniaci, F. Bosia, and N. M. Pugno, Coupling local resonance with Bragg band gaps in single-phase mechanical metamaterials, Extreme Mech. Lett. **12,** 30 (2017).

[6] M. N. Armenise, C. E. Campanella, C. Ciminelli, F. Dell'Olio, and V. M. Passaro, Phononic and photonic band gap structures: Modelling and applications, Phys. Procedia **3,** 357 (2010).

[7] H.-S. Park and J.-H. Han, Design of patch-shaped lens with thickness variations for elastic wave focusing in thin-plate structures, J. Phys. D: Appl. Phys. **57,** 245502 (2024).

[8] J. Jiao, T. Chen, and D. Yu, Observation of topological valley waveguide transport of elastic waves in snowflake plates, Compos. Struct. **286,** 115297 (2022).

[9] M. Miniaci and R. Pal, Design of topological elastic waveguides, J. Appl. Phys. **130,** 141101 (2021).

[10] S.-Y. Yu, C. He, Z. Wang, F.-K. Liu, X.-C. Sun, Z. Li, H.-Z. Lu, M.-H. Lu, X.-P. Liu, and Y.-F. Chen, Elastic pseudospin transport for integratable topological phononic circuits, Nat. Commun. **9,** 3072 (2018).

[11] S. H. Mousavi, A. B. Khanikaev, and Z. Wang, Topologically protected elastic waves in phononic metamaterials, Nat. Commun. **6,** 8682 (2015).

[12] S.-C. S. Lin, T. J. Huang, J.-H. Sun, and T.-T. Wu, Gradient-index phononic crystals, Phys. Rev. B **79,** 094302 (2009).

[13] D. Lee, Y. Hao, J. Park, I. S. Kang, S.-H. Kim, J. Li, and J. Rho, Singular lenses for flexural waves on elastic thin curved plates, Phys. Rev. Appl. **15,** 034039 (2021).

[14] A. Zareei, A. Darabi, M. J. Leamy, and M.-R. Alam, Continuous profile flexural grin lens: Focusing and harvesting flexural waves, Appl. Phys. Lett. **112,** 023901 (2018).

[15] R. Fuentes-Domínguez, M. Yao, A. Colombi, P. Dryburgh, D. Pieris, A. Jackson-Crisp, D. Colquitt, A. Clare, R. J. Smith, and M. Clark, Design of a resonant Luneburg lens for surface acoustic waves, Ultrasonics **111,** 106306 (2021).

[16] A. Climente, D. Torrent, and J. Sánchez-Dehesa, Gradient index lenses for flexural waves based on thickness variations, Appl. Phys. Lett. **105,** 064101 (2014).

[17] Y. Jin, B. Djafari-Rouhani, and D. Torrent, Gradient index phononic crystals and metamaterials, Nanophotonics **8,** 685 (2019).

[18] S. Yang, J. H. Page, Z. Liu, M. L. Cowan, C. T. Chan, and P. Sheng, Focusing of sound in a 3D phononic crystal, Phys. Rev. Lett. **93,** 024301 (2004).

[19] K. Imamura and S. Tamura, Negative refraction of phonons and acoustic lensing effect of a crystalline slab, Phys. Rev. B **70,** 174308 (2004).

[20] R. Zhu, X. Liu, G. Hu, C. Sun, and G. Huang, Negative refraction of elastic waves at the deep-subwavelength scale in a single-phase metamaterial, Nat. Commun. **5,** 5510 (2014).

[21] A. Sukhovich, B. Merheb, K. Muralidharan, J. O. Vasseur, Y. Pennec, P. A. Deymier, and J. Page, Experimental and theoretical evidence for subwavelength imaging in phononic crystals, Phys. Rev. Lett. **102,** 154301 (2009).

[22] J. Christensen and F. J. G. de Abajo, Anisotropic metamaterials for full control of acoustic waves, Phys. Rev. Lett. **108,** 124301 (2012).

[23] X. Cui, J. Zhao, O. Boyko, B. Bonello, and Z. Zhong, Multi-branch subwavelength focusing of the lowest-order antisymmetric Lamb mode in a gradient-index phononic crystal, Int. J. Mech. Sci. **157,** 677 (2019).

[24] M. Antonacci, E. Riva, A. Frangi, A. Corigliano, and V. Zega, Planar grin lenses: Numerical modeling and experimental validation, J. Sound Vib. **537,** 117217 (2022).

[25] T.-T. Wu, Y.-T. Chen, J.-H. Sun, S.-C. S. Lin, and T. J. Huang, Focusing of the lowest antisymmetric Lamb wave in a gradient-index phononic crystal plate, Appl. Phys. Lett. **98,** 171911 (2011).

[26] E. Akmansoy, E. Centeno, K. Vynck, D. Cassagne, and J.-M. Lourtioz, Graded photonic crystals curve the flow of light: An experimental demonstration by the mirage effect, Appl. Phys. Lett. **92,** 133501 (2008).

[27] H. Huang, X. Mao, S.-C. S. Lin, B. Kiraly, Y. Huang, and T. J. Huang, Tunable two-dimensional liquid gradient refractive index (L-GRIN) lens for variable light focusing, Lab Chip **10,** 2387 (2010).

[28] C. Gomez-Reino, M. V. Perez, and C. Bao, *Gradient-Index Optics: Fundamentals and Applications* (Springer Science & Business Media, Berlin Heidelberg, 2012).

[29] J. Hyun, W. Choi, and M. Kim, Gradient-index phononic crystals for highly dense flexural energy harvesting, Appl. Phys. Lett. **115,** 173901 (2019).

[30] J. Zhao, X. Cui, B. Bonello, B. Djafari-Rouhani, W. Yuan, Y. Pan, J. Ren, X. Zhang, and Z. Zhong, Broadband subdiffraction and ultra-high energy density focusing of elastic waves in planar gradient-index lenses, J. Mech. Phys. Solids **150,** 104357 (2021).

[31] S. Tol, F. L. Degertekin, and A. Erturk, Gradient-index phononic crystal lens-based enhancement of elastic wave energy harvesting, Appl. Phys. Lett. **109,** 063902 (2016).

[32] S. Tol, F. Degertekin, and A. Erturk, 3D-printed phononic crystal lens for elastic wave focusing and energy harvesting, Addit. Manuf. **29,** 100780 (2019).

[33] V. Zega, M. Antonacci, A. Frangi, A. Corigliano, and E. Riva, in *2022 Joint Conference of the European Frequency and Time Forum and IEEE International Frequency Control Symposium (EFTF/IFCS)* (IEEE, 2022), p. 1.

[34] G. Lee, J. Park, W. Choi, B. Ji, M. Kim, and J. Rho, Achromatic elastic metalens for high-performance confocal piezoelectric energy harvesting, Appl. Phys. Lett. **123,** 081705 (2023).

[35] S. Tol, F. L. Degertekin, and A. Erturk, Phononic crystal Luneburg lens for omnidirectional elastic wave focusing and energy harvesting, Appl. Phys. Lett. **111,** 013503 (2017).

[36] Y. Jin, D. Torrent, Y. Pennec, Y. Pan, and B. Djafari-Rouhani, Gradient index devices for the full control of elastic waves in plates, Sci. Rep. **6**, 24437 (2016).

[37] J. Park, D. Lee, and J. Rho, Recent advances in nontraditional elastic wave manipulation by macroscopic artificial structures, Appl. Sci. **10**, 547 (2020).

[38] T.-X. Ma, Z.-Y. Li, C. Zhang, and Y.-S. Wang, Energy harvesting of Rayleigh surface waves by a phononic crystal Luneburg lens, Int. J. Mech. Sci. **227**, 107435 (2022).

[39] G. Lefebvre, M. Dubois, R. Beauvais, Y. Achaoui, R. Kiri, S. Guenneau, and P. Sebbah, Experiments on Maxwell's fish-eye dynamics in elastic plates, Appl. Phys. Lett. **106**, 024101 (2015).

[40] G. Lefebvre, M. Dubois, Y. Achaoui, R. Kiri, M. Fink, S. Guenneau, and P. Sebbah, Subwavelength pulse focusing and perfect absorption in the Maxwell fish-eye, Appl. Phys. Lett. **123**, 132203 (2023).

[41] R. Merlin, Maxwell's fish-eye lens and the mirage of perfect imaging, J. Opt. **13**, 024017 (2011).

[42] U. Leonhardt, Perfect imaging without negative refraction, New J. Phys. **11**, 093040 (2009).

[43] Y. G. Ma, S. Sahebdivan, C. Ong, T. Tyc, and U. Leonhardt, Subwavelength imaging with materials of in-principle arbitrarily low index contrast, New J. Phys. **14**, 025001 (2012).

[44] J. Hyun, M. Kim, and W. Choi, Partitioned gradient-index phononic crystals for full phase control, Sci. Rep. **10**, 14630 (2020).

[45] D. Halliday, R. Resnick, and J. Walker, *Fundamentals of Physics* (John Wiley & Sons, New York, 2013).

[46] F. Ma, Z. Huang, C. Liu, and J. H. Wu, Acoustic focusing and imaging via phononic crystal and acoustic metamaterials, J. Appl. Phys. **131**, 011103 (2022).

[47] A. E. H. Love, XVI. The small free vibrations and deformation of a thin elastic shell, Philos. Trans. R. Soc. London A **43**, 491 (1888).

[48] M. Born and E. Wolf, *Principles of Optics: Electromagnetic Theory of Propagation, Interference and Diffraction of Light* (Cambridge University Press, Cambridge, 2013).

[49] G. B. Airy, On the diffraction of an object-glass with circular aperture, Trans. Cambridge Philos. Soc. **5**, 283 (1835).

[50] F. L. Pedrotti, L. M. Pedrotti, and L. S. Pedrotti, *Introduction to Optics* (Cambridge University Press, Cambridge, 2017).

[51] C. H. Wang and F.-K. Chang, Scattering of plate waves by a cylindrical inhomogeneity, J. Sound. Vib. **282**, 429 (2005).